



Self-assembled synthesis of defect-engineered graphitic carbon nitride nanotubes for efficient conversion of solar energy



Zhao Mo^a, Hui Xu^{a,*}, Zhigang Chen^a, Xiaojie She^a, Yanhua Song^b, Jingjie Wu^c, Pengcheng Yan^a, Li Xu^a, Yucheng Lei^a, Shouqi Yuan^a, Huaming Li^{a,*}

^a School of Materials Science & Engineering, Institute for Energy Research, Jiangsu University, Zhenjiang 212013, PR China

^b School of Environmental and Chemical Engineering, Jiangsu University of Science and Technology, Zhenjiang 212003, PR China

^c Department of Chemical and Environmental Engineering, University of Cincinnati, Cincinnati, OH 45221, USA

ABSTRACT

High-yield and uniform-size graphitic carbon nitride nanotubes ($\text{g-C}_3\text{N}_4$ nanotubes) with abundant nitrogen defects are synthesized for the first time by a green and acid-alkali-free synthesis using a sole melamine precursor. This approach utilizes the slow in-situ conversion of part of melamine into cyanuric acid and consequent molecular self-assembly with the rest of melamine to form supramolecular intermediate. The following pyrolysis converts the supramolecular intermediate to $\text{g-C}_3\text{N}_4$ nanotubes with abundant nitrogen defects. The morphology thus resulted preferable performance than the traditional molecular self-assembly in which the mixture of melamine and cyanuric acid is used as precursors. The $\text{g-C}_3\text{N}_4$ nanotubes with orderly tubular morphology of length-diameter ratio of 30–70 exhibit excellent hydrogen evolution rate ($118.5 \mu\text{mol h}^{-1}$), which is obviously superior to the bulk $\text{g-C}_3\text{N}_4$. The apparent quantum efficiency of $\text{g-C}_3\text{N}_4$ nanotubes under irradiation at 420 nm is achieved at 6.8%, which is among the top of one dimensional (1D) $\text{g-C}_3\text{N}_4$ structure, such as $\text{g-C}_3\text{N}_4$ nanotubes, nanowires and nanorods. The improved photocatalytic performance benefits from the tubular structure and the nitrogen defects, which lead to the improved optical absorption, more exposed active edges, nitrogen defects active sites, enhanced charge transfer and separation efficiency, higher surface area, fast and long-distance electron transport, and longer fluorescence lifetime. Beside hydrogen evolution reaction, the $\text{g-C}_3\text{N}_4$ nanotubes also have broad applications in environmental treatment and photoelectrochemical detection of organic dyes.

1. Introduction

As a nonmetallic semiconductor material, graphitic carbon nitride ($\text{g-C}_3\text{N}_4$) not only possesses suitable band gap (2.7 eV) to effectively utilize the visible light ($\lambda < 470 \text{ nm}$), but also has excellent physical and chemical properties, such as good chemical tenability, thermal stability, commendable photoelectric properties and powerful antioxidant property [1,2]. Therefore, $\text{g-C}_3\text{N}_4$ has been generally applied in photocatalytic water splitting, pollutants degradation, artificial photosynthesis and CO_2 reduction [3–5]. However, the bulk $\text{g-C}_3\text{N}_4$ prepared by traditional calcination thermal condensation of precursors (melamine [6], dicyanodiamine [7], thiourea [8], urea [9]) has many fatal shortcomings, such as high recombination rate of the photogenerated electron-hole pairs, slow transfer rate of the charge carriers, limited active sites, insufficient photoabsorption and low surface area, which seriously restrict its further development to practical application [10–13]. In order to further enhance the photocatalytic performance of the bulk $\text{g-C}_3\text{N}_4$, the following strategies are widely explored, including nanostructure design, element doping, constructing heterojunction with other

semiconductor materials and in situ defect modification of $\text{g-C}_3\text{N}_4$ [14–19]. Particularly, nanostructure design of $\text{g-C}_3\text{N}_4$, like porous, hierarchical, nanosheet, nanorod, nanotube and quantum dot structure, is indeed a promising approach to solve its own short-board problem [18,20–22]. At the same time, nanostructure design can also introduce abundant defects into $\text{g-C}_3\text{N}_4$.

Especially for $\text{g-C}_3\text{N}_4$ nanotubes, they have both hollow and 1D structure at the same time, which bring some unique advantages in photocatalytic reaction, like enhanced visible light absorption and scattering ability, fast and long-distance electron transport, more abundant active sites, larger specific surface area, and lower recombination rate of photogenerated electron-hole pairs [23–25]. The major preparation methods of $\text{g-C}_3\text{N}_4$ nanotubes include hard-templating method, soft-templating method and self-templating method [26–28]. The hard-templating method is the most common way to synthesize $\text{g-C}_3\text{N}_4$ nanotubes, which usually chooses porous anodic aluminum oxide (AAO), ordered mesoporous silica as the template [29]. The hard-templating method can actually enlarge the surface area of $\text{g-C}_3\text{N}_4$, for which it is considered as an efficient way for preparing $\text{g-C}_3\text{N}_4$.

* Corresponding authors.

E-mail addresses: xh@ujs.edu.cn (H. Xu), lihm@ujs.edu.cn (H. Li).

nanotubes. However, the method has the long preparation cycle and complicated steps. Meanwhile, the strongly corrosive HF or NH_4HF_2 is usually used to remove the template in the synthesis process, which is unfriendly to environment and dangerous. In addition, the soft-templating method has the advantages of simple operation, cheap prices, which uses surfactants, ionic liquids and so on [30]. But the soft-templating method also has many problems, such as bad structural stability and low efficiency. The biggest challenges of the soft-templating method are the removal of the template agent. Therefore, it is of great necessity to explore a facile and high-yield method for the fabrication of $\text{g-C}_3\text{N}_4$ nanotubes. Molecular self-assembly has already been commonly used as a self-templating method to prepare nanostructure materials [31–37]. Taking $\text{g-C}_3\text{N}_4$ as example, the specific morphology of $\text{g-C}_3\text{N}_4$ can be obtained by directly heating the supramolecular intermediate. So, the morphology and structure of supramolecular intermediate are very important to get the $\text{g-C}_3\text{N}_4$ with special structure. The supramolecular intermediate is formed due to the interaction between the hydrogen bonds. The hydrogen bonds in the supramolecular self-assembly process are crucial to form the ordered structure of the supramolecular intermediate, since hydrogen bonding has strong saturation and direction [35,38]. At the same time, it is worth noting that the specific morphology of $\text{g-C}_3\text{N}_4$ usually has a positive impact on the photocatalytic performance. However, the reported molecular self-assembly of $\text{g-C}_3\text{N}_4$ generally using two or more of the raw materials, especially dimethyl sulfoxide, chloroform and other organic solvents as the reaction solvent, which can't reflect the green and environmental protection concept [31–37,39–43]. Meanwhile, the morphology of the obtained supramolecular intermediate is irregular, which has a negative impact on the morphology of the final materials. In addition, few studies on $\text{g-C}_3\text{N}_4$ nanotubes with molecular self-assembly have been researched previously.

In this work, we utilize an efficient self-assembled approach to obtain the high-yield defect-engineered $\text{g-C}_3\text{N}_4$ nanotubes without any templates and surfactants. It's worth noting that, the starting materials used in this study are fairly simple, just a sole melamine. The formation mechanism of the rod-like supramolecular intermediate and the formation process of the $\text{g-C}_3\text{N}_4$ nanotubes are discussed. The $\text{g-C}_3\text{N}_4$ nanotubes exhibit enhanced photocatalytic activity for hydrogen evolution. Its hydrogen evolution rate is up to $118.5 \mu\text{mol h}^{-1}$ and the quantum efficiency at 420 nm is 6.8% (in the front rank of 1D $\text{g-C}_3\text{N}_4$ reported to date). Chief causes of the enhanced photocatalytic performance are the own strengths of the tubular structure and the nitrogen defects. In addition, $\text{g-C}_3\text{N}_4$ nanotubes also can be used for the environmental treatment and the photoelectrochemical detection of MB.

2. Experimental

2.1. Synthesis of $\text{g-C}_3\text{N}_4$ nanotubes

This synthetic approach of $\text{g-C}_3\text{N}_4$ nanotubes is a two-step process. First, melamine (2 g) is added into deionized water (40 mL) with strong stirring for 2 h. The mixture solution is transferred into a Teflon lined autoclave at 200°C for 4, 8, 12 and 16 h. The obtained supramolecular intermediate is washed several times with deionized water and dried at 60°C . Secondly, the supramolecular intermediate is heated to 550°C in a muffle furnace for 4 h with a heating rate of $2^\circ\text{C}/\text{min}$. The final product can be chosen for future use without further ground in an agate mortar. As a comparison, the bulk $\text{g-C}_3\text{N}_4$ is prepared by calcining melamine (2 g) directly at 550°C in a muffle furnace for 4 h with a heating rate of $2^\circ\text{C}/\text{min}$.

2.2. Photocatalytic activity measurement

The photocatalytic hydrogen production reaction is carried out in an online photocatalytic hydrogen production system (LbSolar-3AG, PerfectLight, Beijing). 0.01 g of photocatalysts is added into aqueous solution (90 mL water and 10 mL hole sacrificial agent). Then, Pt nanoparticles are added by the in-situ photodeposition ($3 \text{ wt\% H}_2\text{PtCl}_6 \cdot 6\text{H}_2\text{O}$). Next, the solution is degassed and irradiated by a 300 W Xenon lamp (PLS-SXE 300C (BF), PerfectLight, Beijing) with an optical filter ($\lambda > 400 \text{ nm}$). The H_2 evolution rate is determined using an online gas chromatograph (GC

D7900P, TCD detector, N_2 carrier, 5A molecular sieve column, Shanghai Fehcomp).

3. Results and discussion

3.1. Self-assembly of the rod-like supramolecular intermediate from melamine

Fig. 1 shows the morphological evolution of the supramolecular intermediate during hydrothermal reaction. The SEM image of the melamine (Fig. 1a) shows that the melamine displays the originally irregular shapes. Clearly seen from Fig. 1b–d, the microstructure of the supramolecular intermediate gradually turns into regular rod-like structure from the original structure, along with the extension of hydrothermal reaction time from 4 h to 12 h at 200°C in deionized water. As shown in Fig. 1d, the supramolecular intermediate exhibits a fairly good rod-like structure with a diameter of $1\text{--}2 \mu\text{m}$ when the hydrothermal reaction time is 12 h. However, once the hydrothermal reaction time increases to 16 h, the rod-like intermediate fuses and aggregates (Fig. 1e). This may be for the reason that some hydrogen bonds of supramolecular intermediate are broken, that is, supramolecular intermediate will further react with H_2O . The above results indicate that the supramolecular intermediate can readily form the rod-like structure by adjusting the hydrothermal reaction time. The formation of the rod-like supramolecular intermediate is possibly through the self-assembly mechanism as illustrated in the left side of Scheme 1. Self-assembly of the rod-like supramolecular intermediate is successfully achieved via one-pot hydrothermal reaction of the melamine, which is the most essential link for forming $\text{g-C}_3\text{N}_4$ nanotubes during the whole process. Firstly, part of the melamine is turned into cyanuric acid by heating at 200°C for 12 h, and accompanied with a release of NH_3 (Scheme S1a). When opening the cover of autoclave, a stream of strong pungent odor can be smelt which proves the production of NH_3 . The released NH_3 may cause the increasing of the pH, as shown in Fig. S1a. The pH value before hydrothermal reaction is 8.25, while the pH value after hydrothermal reaction is 9.76 (Fig. S1b). The pH rising can further indicate the production of NH_3 . Secondly, the generated cyanuric acid immediately combines with the rest of the melamine by hydrogen bonding to form the supramolecular intermediate (Scheme S1b). Specifically, one melamine molecule can generate three hydrogen bonds with the cyanuric acid molecule, and one cyanuric acid molecule can also form three hydrogen bonds with the melamine molecule. So the rod-like supramolecular intermediate is formed through the self-assembly of melamine molecule and cyanuric acid molecule via hydrogen bonding. Meanwhile, the released NH_3 also plays an auxiliary role in the formation process of the rod-like supramolecular intermediate [44,45].

To further prove the successful formation of the proposed supramolecular intermediate, the XRD and IR analyses are used (see Fig. S2). The diffraction peaks (Fig. S2a) of the supramolecular intermediate observed at 11.8° , 17.7° and 21.9° are assigned to (100) plane, (110) plane, and (200) plane of the in-planar packing, respectively. In addition, the peak (002) at 28.1° is attributed to the graphite-like stacking of sheet-like structure [36]. The XRD pattern is consistent with that in the previous report [32], which can serve as a significant evidence for the formation of the supramolecular intermediate. No obvious diffraction peaks of the melamine can be observed in the supramolecular intermediate, which attests that melamine has totally transformed into the supramolecular intermediate. The supramolecular intermediate is further investigated by FT-IR analysis (Fig. S2b). As compared with the triazine ring vibration of melamine at 809 cm^{-1} , the triazine ring vibration of the supramolecular intermediate is shifted to a lower frequency at 768 cm^{-1} . It has been reported that the $\text{C}=\text{O}$ stretching vibration of cyanuric acid is at 1691 cm^{-1} [36], while the supramolecular intermediate is shifted to a higher wavenumber at 1732 cm^{-1} . The shift of triazine ring vibration of melamine to a lower wavenumber along with the $\text{C}=\text{O}$ stretching vibration of cyanuric acid to a higher wavenumber is ascribed to the existence of hydrogen bonding $\text{N}-\text{H}\cdots\text{N}$ and $\text{N}-\text{H}\cdots\text{O}$ in the supramolecular intermediate [33,46]. Therefore, the result indicates that a part of the melamine really turns into cyanuric acid at first. Then the generated cyanuric acid combines with the rest of the melamine by hydrogen bonding

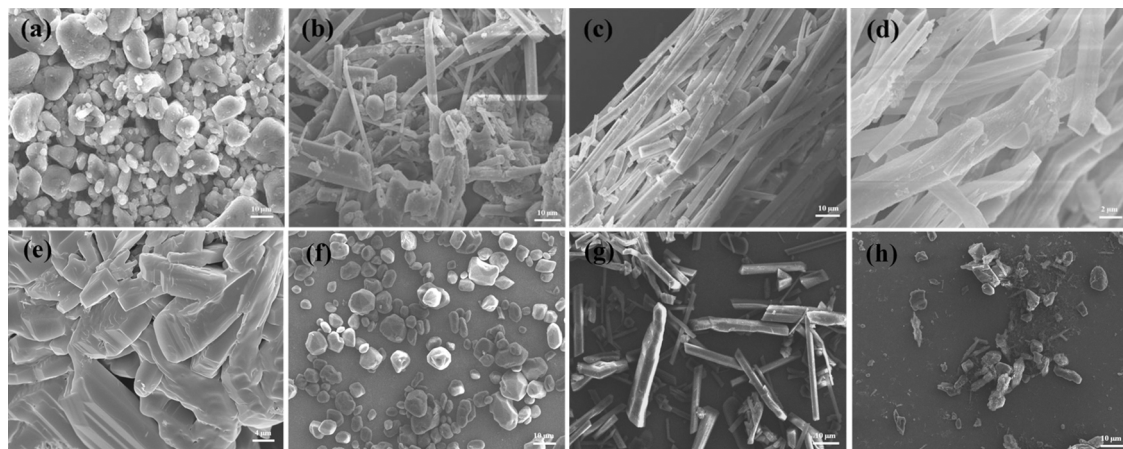
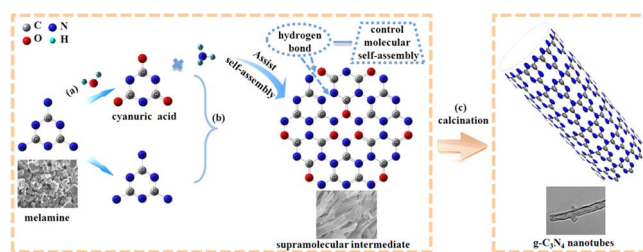


Fig. 1. The SEM images of (a) melamine and the supramolecular intermediate at different hydrothermal reaction time (b) 4 h, (c) 8 h, (d) 12 h, (e) 16 h, the SEM images of melamine by hydrothermal reaction (f) at 160 °C, (g) at 180 °C, (h) in ethanol.



Scheme 1. The formation process of the g-C₃N₄ nanotubes.

to form the supramolecular intermediate.

In order to investigate the effect of temperature and solvent, the control hydrothermal experiments (Fig. S2c, S2d) are also operated. When the hydrothermal reaction temperature is set at 160 °C for 12 h using deionized water as the solvent, or at 200 °C for 12 h choosing ethanol as the solvent, XRD pattern and FT-IR spectra of both samples are in good accordance with melamine except the intensity of peaks. The results confirm that melamine doesn't partly turn into cyanuric acid that links the remainder melamine to form the supramolecular intermediate. As the hydrothermal reaction temperature reaches 180 °C, the weak peaks of the supramolecular intermediate are observed, but the melamine is still the main component. Glycol is also used as the solvent, and the hydrothermal reaction temperature is set at 200 °C for 12 h, but no precipitate can be found in the autoclave. Therefore, the hydrothermal reaction time, temperature and solvent are of great importance for the formation of the rod-like supramolecular intermediate. The SEM images of the samples by hydrothermal reaction at 160 °C, at 180 °C, and in ethanol are further investigated in Fig. 1f–h. Compared to melamine, the microstructure of sample heating at 160 °C (Fig. 1f) does not change much, just become relatively homogeneous. As shown in Fig. 1g, the sample heating at 180 °C shows rod-like structure of various lengths and diameters. When ethanol is chosen as the hydrothermal reaction solvent (Fig. 1h), no significant change of the microstructure is observed compared to that of melamine. So synthesizing the above investigations of the hydrothermal reaction temperature, time and solvent, the conclusions are as followed. First, the choice of solvent determines whether the supramolecular intermediate will be formed or not. Only when deionized water is employed in the hydrothermal reaction can part of the melamine turn into cyanuric acid which in turn links with the rest of the melamine to form the supramolecular intermediate. Next, the hydrothermal reaction time and temperature are also very important to form regular rod-like supramolecular intermediate. Only when the hydrothermal temperature reaches to sufficiently high value (200 °C) can the supramolecular intermediate be formed. Besides, sufficiently long reaction time (12 h) is essential to the formation of regular rod-like supramolecular intermediate. Furthermore, choice of melamine rather than a mixture of melamine and cyanuric acid as the starting material is very

important for the formation of regular rod-like supramolecular intermediate, because melamine can in situ turn into cyanuric acid at a rather slow rate.

3.2. Formation of the defect-engineered g-C₃N₄ nanotubes

The formation process of defect-engineered g-C₃N₄ nanotubes is shown in Scheme 1. After the thermal treatment, the rod-like supramolecular intermediates are transformed into the g-C₃N₄ nanotubes. The g-C₃N₄ nanotubes possess a length of several microns and a diameter of 30–60 nm with an aspect ratio of 30–70 as shown in Fig. 2a. The length and diameter of the g-C₃N₄ nanotubes are much smaller than that of the rod-like supramolecular intermediate, which may be due to the thermal condensation of the supramolecular intermediate. The tubular structure can enhance the specific surface area and provide multiple light reflection/scattering channels resulting in fast and long-distance electron transport, more exposed active edges, and enhanced light absorption, which all contribute to the improvement of the photocatalytic performance [47]. The TEM image of Fig. 2b further confirms that the g-C₃N₄ nanotubes are successfully gained as expected. As shown in the magnified TEM image, the wall of g-C₃N₄ nanotubes is composed of several layers, and the wall thickness is about 15 nm (Fig. 2c). The specific surface area of g-C₃N₄ nanotubes is further investigated by the nitrogen adsorption and desorption isotherm. As can be seen in Fig. 2d, the BET surface area of the g-C₃N₄ nanotubes attains approximately 127.8 m² g⁻¹, which is about 14.9 times higher than that of the bulk g-C₃N₄ in our previous report (8.6 m² g⁻¹) [48]. Meanwhile, it can be seen from the inset of Fig. 2d, the pore size of the g-C₃N₄ nanotubes is mainly 30–60 nm, which is in accordance with the diameter in TEM observation.

The possible mechanism for the formation of the g-C₃N₄ nanotubes is proposed as the NH₃-template assisted rolling-up mechanism [44,49–51], that is the rod-like supramolecular intermediate acts as the self-template for the synthesis of the g-C₃N₄ nanotubes. During the thermal condensation stage, a mass of NH₃ is released because of the pyrolysis of the supramolecular intermediate. The generated NH₃ can go through the supramolecular intermediate to form a tube-like structure. The supramolecular intermediate will gradually contract and roll with the increase of calcination temperature, which results in the smaller diameter of the final product than that of the supramolecular intermediate.

The crystal structure of the g-C₃N₄ nanotubes is investigated by XRD. As depicted in Fig. 3a, for the bulk g-C₃N₄, the (100) plane at around 13.1° relates to the in-plane structural packing motif of tri-*s*-triazine units, and the (002) plane at 27.3° corresponds to the characteristic inter-planar stacking reflection of conjugated aromatic systems [48,52]. Compared to the XRD pattern of bulk g-C₃N₄, the (100) peak of the g-C₃N₄ nanotubes can be barely observed, which indicates that the g-C₃N₄ nanotubes possess the smaller planar size of the layers [53,54]. Meanwhile, the intensity of (002) peak becomes weaker, which may be attributed to the evident size dependent properties of the g-C₃N₄ nanotubes [32]. As shown in Fig. 3b, the chemical

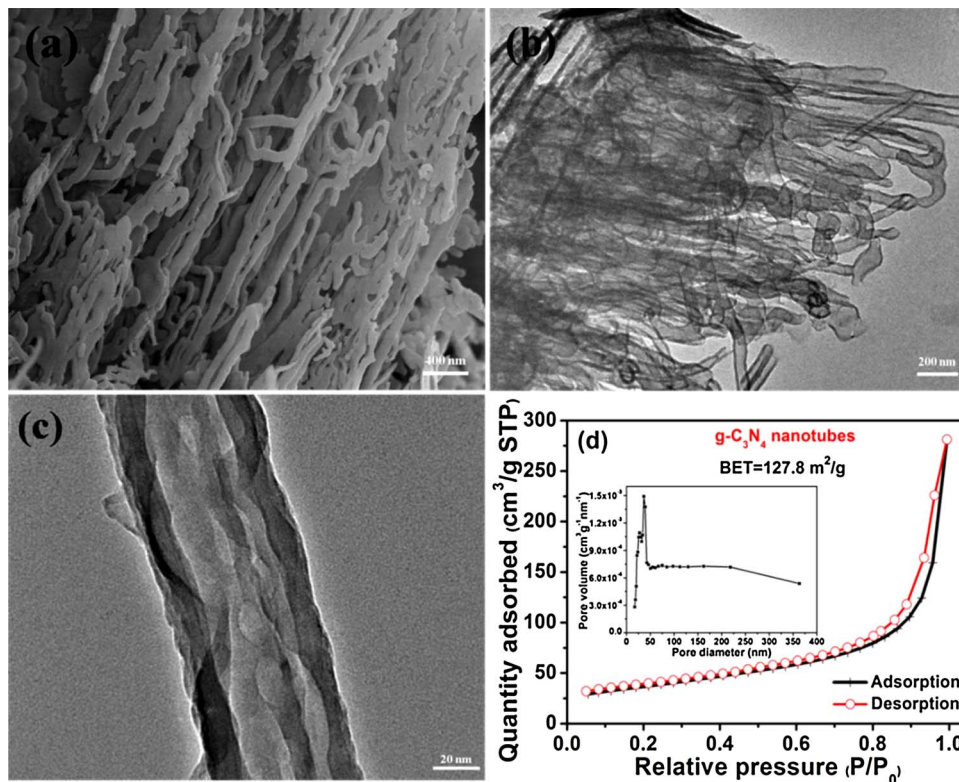


Fig. 2. (a) The SEM images of the $\text{g-C}_3\text{N}_4$ nanotubes, (b) the detailed TEM images of the $\text{g-C}_3\text{N}_4$ nanotubes, (c) The magnified TEM image of the $\text{g-C}_3\text{N}_4$ nanotubes, (d) Nitrogen absorption-desorption isotherm of the $\text{g-C}_3\text{N}_4$ nanotubes, Inset: the pore size distribution of the $\text{g-C}_3\text{N}_4$ nanotubes.

structure of the $\text{g-C}_3\text{N}_4$ nanotubes is further analyzed by FT-IR spectra. All the IR bands of the $\text{g-C}_3\text{N}_4$ nanotubes are in good accordance with the bulk $\text{g-C}_3\text{N}_4$, which manifests that the chemical structure of the $\text{g-C}_3\text{N}_4$ nanotubes is nearly identical to that of bulk $\text{g-C}_3\text{N}_4$. The band at about 812 cm^{-1} corresponds to the characteristic breathing mode of the *s*-triazine units [55]. The absorption bands observed at about 1241, 1326, 1412, 1564 and 1640 cm^{-1} are assigned to the typical stretching vibration modes of CN heterocycles [56]. It is worth noting that an enhanced absorption between 3600 cm^{-1} and 3000 cm^{-1} of the $\text{g-C}_3\text{N}_4$ nanotubes can be observed obviously, which corresponds to the surface-bonded H_2O molecules and amino groups, indicating the $\text{g-C}_3\text{N}_4$ nanotubes have the enlarged open-up surfaces [54,57].

To confirm the existence of nitrogen defects inside the $\text{g-C}_3\text{N}_4$ nanotubes, four analytical methods are synthetically utilized. Firstly, elemental analysis (EA) is employed to certify the existence of nitrogen defects inside the $\text{g-C}_3\text{N}_4$ nanotubes. The composition of C, N, and H in the $\text{g-C}_3\text{N}_4$ nanotubes is shown in Table 1. The result indicates that the C/N atomic ratio of $\text{g-C}_3\text{N}_4$ nanotubes is higher than that of the bulk $\text{g-C}_3\text{N}_4$. EA confirms that nitrogen defects are generated on the $\text{g-C}_3\text{N}_4$ nanotubes by treating the supramolecular intermediates. Second, the X-ray photoelectron spectroscopy (XPS) studies further indicate the formation of nitrogen defects. Fig. 3c shows the survey XPS spectra of the bulk $\text{g-C}_3\text{N}_4$ and the $\text{g-C}_3\text{N}_4$ nanotubes, which exhibit similar features. C, N and O elements are all found in the two samples, indicating that the $\text{g-C}_3\text{N}_4$ nanotubes maintain the same chemical composition and chemical states with the bulk $\text{g-C}_3\text{N}_4$. However, compared with the C/N atomic ratio of the bulk $\text{g-C}_3\text{N}_4$, $\text{g-C}_3\text{N}_4$ nanotubes show an evident increase (Table S1). This result indicates the loss of N atoms via heating the supramolecular intermediates, which is consistent with the result of EA, confirming the existence of nitrogen defects inside the $\text{g-C}_3\text{N}_4$ nanotubes. The high-resolution C 1s spectrum in Fig. 3d can be fitted with two peaks at about 284.8 and 288.3 eV. The peak at 284.8 eV corresponds to adsorbed carbon, while peak at 288.3 eV is assigned to the typical aromatic N–C–N coordination [58,59]. As shown in Fig. 3e, the high-resolution N 1s spectrum can be deconvoluted into three peaks at about 398.8, 400.4 and 401.5 eV, which are attributed to nitrogen atoms in the $\text{sp}^2\text{C}=\text{N}–\text{C}$, $\text{sp}^3\text{C}–\text{N}(\text{–C})–\text{C}$ and C–N–H functional groups, respectively [60]. In order to investigate which form of the nitrogen species is preferentially lost, the high-resolution C 1s spectrum and N 1s spectrum are provided and the bonding

ratios of the different nitrogen species are shown in Table S2. The content of $\text{sp}^2\text{C}=\text{N}–\text{C}$ bonds for the $\text{g-C}_3\text{N}_4$ nanotubes is far above that of the bulk $\text{g-C}_3\text{N}_4$. In contrast the content of $\text{sp}^3\text{C}–\text{N}(\text{–C})–\text{C}$ is considerably reduced. For $\text{g-C}_3\text{N}_4$ nanotubes, the ratio of $\text{sp}^2\text{C}=\text{N}–\text{C}$ bonds to the sum of $\text{sp}^3\text{C}–\text{N}(\text{–C})–\text{C}$ and C–N–H is far above that of the bulk $\text{g-C}_3\text{N}_4$. Because $\text{sp}^3\text{C}–\text{N}(\text{–C})–\text{C}$ and C–N–H represents the total amount of protons, the $\text{g-C}_3\text{N}_4$ nanotubes have lower proton concentration leading to higher photocatalytic activity [54,61]. In addition, ^{15}N solid-state NMR spectroscopy is also carried out. As depicted in Fig. S3, the signals between -166 and -203 ppm belong to the ring nitrogen of the heptazine ring ($\text{–N}=\text{}$), the weak signals between -208 and -224 ppm are assigned to the center nitrogen ($\text{–N} < \text{}$), the signals between -236 and -252 ppm to the bridging NH groups, and the signals between -253 and -302 ppm belong to the NH_2 groups [14,16]. The $\text{–N} < \text{}$ signals of the $\text{g-C}_3\text{N}_4$ nanotubes show a considerable decrease in the signal intensity compared to the bulk $\text{g-C}_3\text{N}_4$, indicating that the content of $\text{sp}^3\text{C}–\text{N}(\text{–C})–\text{C}$ is clearly reduced, in concordance with XPS results. Finally, electron paramagnetic resonance (EPR) analysis is provided to verify the formation of nitrogen defects [62]. Fig. 3f shows that $\text{g-C}_3\text{N}_4$ nanotubes and bulk $\text{g-C}_3\text{N}_4$ both display a single Lorentzian line at $g = 2.0035$, which is related to the unpaired electrons on the carbon atoms of the aromatic rings [63]. The EPR intensity of the $\text{g-C}_3\text{N}_4$ nanotubes is notably strengthened and broadened compared to that of the bulk $\text{g-C}_3\text{N}_4$, indicating the existence of nitrogen defects in the $\text{g-C}_3\text{N}_4$ nanotubes [62]. Therefore, the generation of nitrogen defects in the $\text{g-C}_3\text{N}_4$ nanotubes has been confirmed by a combination results from XPS, EA, ^{15}N solid-state NMR and EPR.

3.3. Optical absorption properties

The optical property has a great influence on the photocatalytic performance, thus the optical properties of the bulk $\text{g-C}_3\text{N}_4$ and the $\text{g-C}_3\text{N}_4$ nanotubes are studied by the UV-vis diffuse reflectance spectra. As shown in Fig. 4a, the photoabsorption edge of the $\text{g-C}_3\text{N}_4$ nanotubes is found to be red shifted in comparison with that of bulk $\text{g-C}_3\text{N}_4$, owing to the loss of N atoms [64]. Compared with the light absorption of the bulk $\text{g-C}_3\text{N}_4$, the $\text{g-C}_3\text{N}_4$ nanotubes exhibit the enhanced light harvesting ability. This is chiefly ascribed to the multiple reflections of incident light in the tubular structure, which might contribute to improve the photocatalytic activity [65]. The

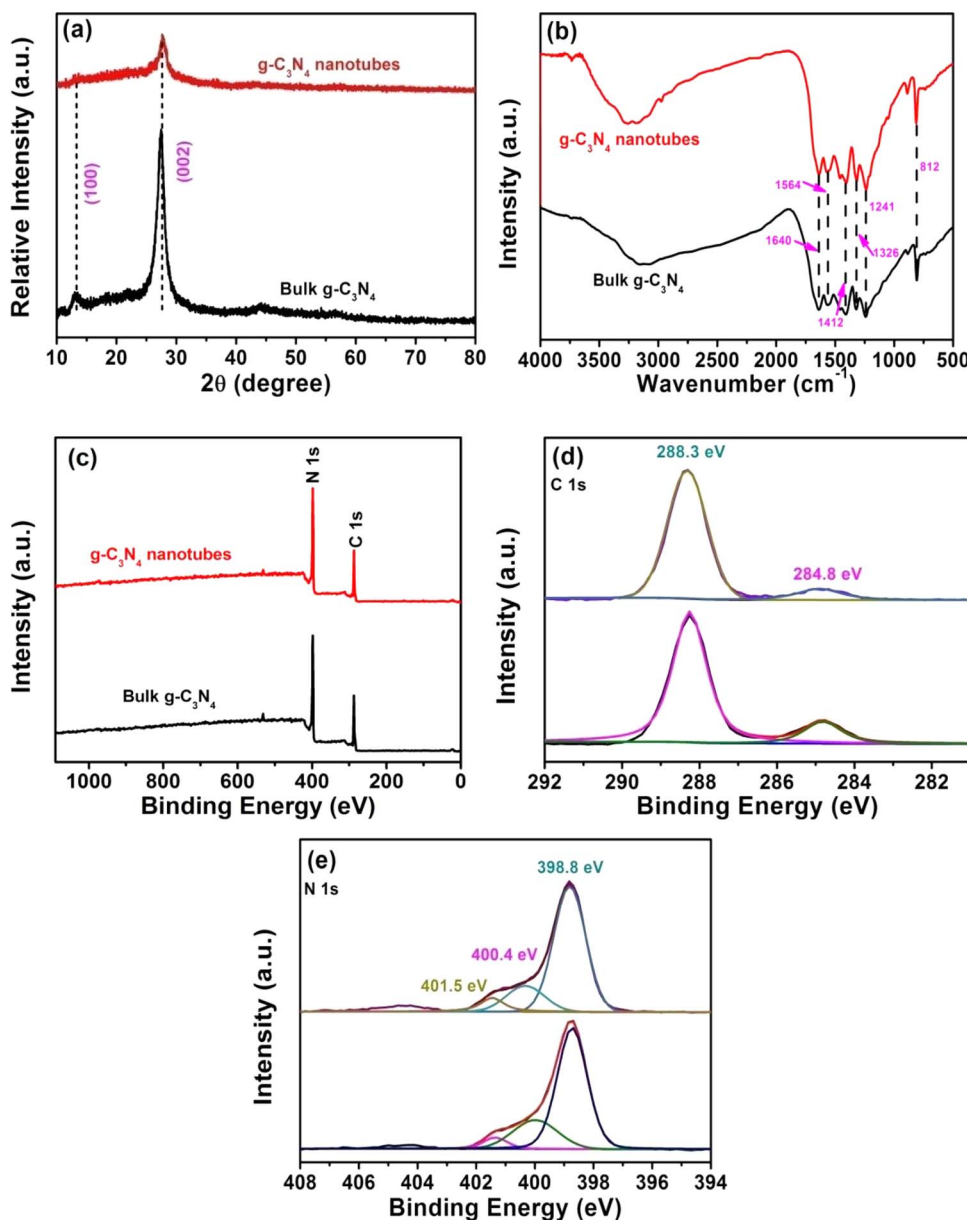


Fig. 3. (a) XRD patterns of the bulk $\text{g-C}_3\text{N}_4$ and the $\text{g-C}_3\text{N}_4$ nanotubes, (b) FT-IR spectra of the bulk $\text{g-C}_3\text{N}_4$ and the $\text{g-C}_3\text{N}_4$ nanotubes, (c) XPS survey spectra (d) C 1s, (e) N 1s of the bulk $\text{g-C}_3\text{N}_4$ and the $\text{g-C}_3\text{N}_4$ nanotubes, (f) electron paramagnetic resonance spectra of the bulk $\text{g-C}_3\text{N}_4$ and the $\text{g-C}_3\text{N}_4$ nanotubes.

Table 1
Composition (wt%) of C, N and H in the bulk $\text{g-C}_3\text{N}_4$ and the $\text{g-C}_3\text{N}_4$ nanotubes.

Samples	Bulk $\text{g-C}_3\text{N}_4$	$\text{g-C}_3\text{N}_4$ nanotubes
C	38.74	40.77
N	55.88	53.81
H	2.41	2.36
C/N atomic ratio	0.693	0.758

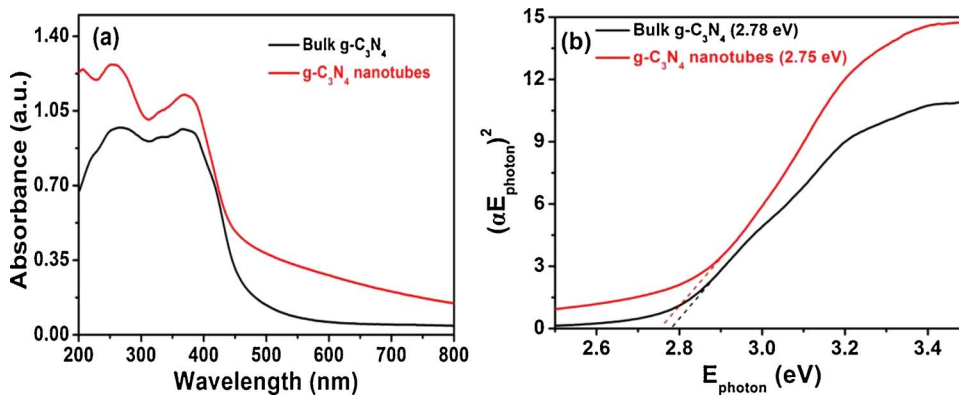
corresponding optical band gaps are extracted as 2.78 and 2.75 eV by fitting (Fig. 4b), which is due to the nitrogen defects in $\text{g-C}_3\text{N}_4$ nanotubes [66].

3.4. Photocatalytic performance

The photocatalytic activity of the $\text{g-C}_3\text{N}_4$ nanotubes is tested by hydrogen evolution from water and pollutants degradation under visible light irradiation. As shown in Fig. 5a, for the $\text{g-C}_3\text{N}_4$ nanotubes, a total amount of $592.5 \mu\text{mol}$ ($118.5 \mu\text{mol h}^{-1}$) H_2 is produced after 5 h visible light irradiation ($\lambda > 400 \text{ nm}$), which is about 12.8 times of H_2 generated by the bulk $\text{g-C}_3\text{N}_4$ ($9.26 \mu\text{mol h}^{-1}$), and is also superior to most of reported 1D $\text{g-C}_3\text{N}_4$

structures [23–25, 32, 35, 42, 67–69]. The stability and recyclability of the photocatalyst are also especially relevant to its practical application. Recycling reactions are tested for hydrogen evolution from water over the $\text{g-C}_3\text{N}_4$ nanotubes under visible light irradiation. Fig. 5a shows that the hydrogen evolution rate of the $\text{g-C}_3\text{N}_4$ nanotubes remain relatively stable after four continuous cycles, which means the $\text{g-C}_3\text{N}_4$ nanotubes have a high degree of photocatalytic stability. At the same time, the $\text{g-C}_3\text{N}_4$ nanotubes also exhibit increased performance of methylene blue (MB), 4-chlorophenol (4-CP) and Bisphenol A (BPA) degradation under visible light irradiation, which can be seen in Fig. S4. Fig. S5b presents the XRD pattern of the $\text{g-C}_3\text{N}_4$ nanotubes before and after the photocatalytic reactions. There is no apparent change in the crystal structures of the sample after hydrogen evolution and pollutants degradation, which indicates that the $\text{g-C}_3\text{N}_4$ nanotubes are very stable in the process of hydrogen evolution from water and pollutants degradation.

The turnover number (TON) of $\text{g-C}_3\text{N}_4$ nanotubes is up to 384.97 by calculation, and its corresponding turnover frequency (TOF) is 76.99 h^{-1} , almost 12.8 times higher than that of the bulk $\text{g-C}_3\text{N}_4$ (Table S3). Fig. 5b gives the apparent quantum efficiency of $\text{g-C}_3\text{N}_4$ nanotubes under the monochromatic light irradiation conditions. The apparent quantum efficiency trend line shows an agreement with the UV-vis diffuse reflectance



spectra. The calculated result shows that the apparent quantum efficiency of $\text{g-C}_3\text{N}_4$ nanotubes under irradiation at 420 nm, 435 nm and 450 nm is 6.8%, 3.1% and 1.7%, respectively, which indicates that hydrogen evolution mainly comes from a range of 400–450 nm.

3.5. Possible photocatalytic mechanism

The enhanced photocatalytic activity of $\text{g-C}_3\text{N}_4$ nanotubes mainly lies in following two aspects: the well-organized tubular structure and the abundant nitrogen defects. The tubular structure can promote the optical absorption, extend the surface area, lead to fast and long-distance electron transport and facilitate transfer and separation efficiency of the photo-generated electron-hole pairs. Furthermore, nitrogen defects can narrow the band gap and act as electron or hole traps to facilitate charge transfer and separation efficiency. Next, the reasons of enhanced photocatalytic activity are discussed in more detail.

The charge transfer and separation efficiency has great influence on the photocatalytic property, which can help better understand the possible photocatalytic mechanism. Therefore the photoluminescence (PL) spectra analysis, the time-resolved fluorescence decay spectra, photocurrents and EIS measurements are performed. Fig. 6a displays the PL spectra of the bulk $\text{g-C}_3\text{N}_4$ and the $\text{g-C}_3\text{N}_4$ nanotubes. The emission peaks are at the same positions centered at around 475 nm, suggesting that the process of forming the supramolecular intermediate does not affect the position of the emission peak. The PL intensity of the $\text{g-C}_3\text{N}_4$ nanotubes is much less than that of the bulk $\text{g-C}_3\text{N}_4$, indicating that the $\text{g-C}_3\text{N}_4$ nanotubes possess a lower recombination rate of the photo-generated electron-hole pairs. And this is possible because the tube-like structure of the $\text{g-C}_3\text{N}_4$ nanotubes with nitrogen defects can create new surface states for charge traps, thus inhibiting the recombination of photo-generated electron-hole pairs [54,70]. The PL results show that the tubular structure and nitrogen defects are conducive to the charge separation and has a lower recombination rate of photo-generated electron-hole pairs, then bringing about higher photoactivity. The electron transfer behavior of the $\text{g-C}_3\text{N}_4$ nanotubes is further investigated by the time-resolved fluorescence decay spectra. As shown in Fig. 6b, the decay phenomenon of $\text{g-C}_3\text{N}_4$ nanotubes is best fitted by the double exponential function:

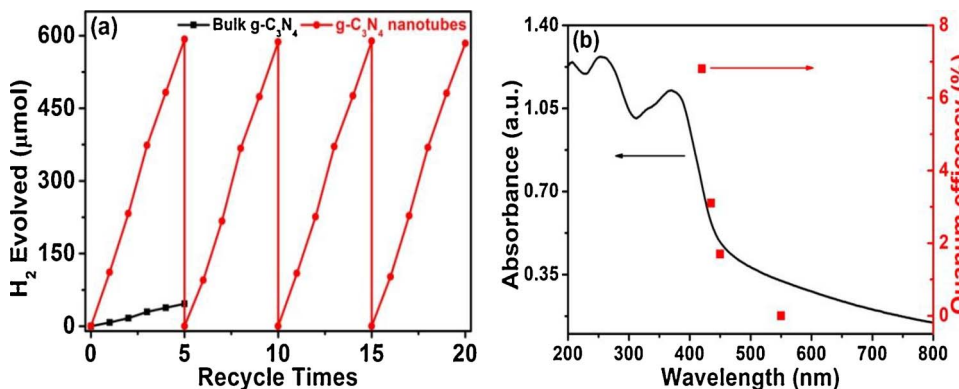


Fig. 4. (a) Optical absorption spectroscopy of the bulk $\text{g-C}_3\text{N}_4$ and the $\text{g-C}_3\text{N}_4$ nanotubes, (b) the estimated band gaps of the bulk $\text{g-C}_3\text{N}_4$ and the $\text{g-C}_3\text{N}_4$ nanotubes.

$$I(t) = A_1 \exp(-t/\tau_1) + A_2 \exp(-t/\tau_2)$$

Where A_1 and A_2 are weighting parameters, τ_1 and τ_2 are the decay lifetime of luminescence, which is summarized in the inset of Fig. 6b [71]. The average lifetime is marked as τ_{av} , which is obtained by the following formula:

$$\tau_{av} = (A_1 \tau_1^2 + A_2 \tau_2^2) / (A_1 \tau_1 + A_2 \tau_2)$$

τ_{av} of the bulk $\text{g-C}_3\text{N}_4$ and the $\text{g-C}_3\text{N}_4$ nanotubes is calculated to be 3.23 ns and 8.06 ns [72]. The average charge lifetime can be used to evaluate the separation efficiency of photogenerated electron-hole pairs [73]. The average charge lifetime of $\text{g-C}_3\text{N}_4$ nanotubes has about 2.50-fold increase over that of the bulk $\text{g-C}_3\text{N}_4$, indicating a lower recombination rate and a higher separation efficiency of photogenerated electron-hole pairs, thus $\text{g-C}_3\text{N}_4$ nanotubes possess more free charges to participate in the surface redox reaction [74]. The thin tubular structure and nitrogen defects promote the migration of photogenerated electrons to the surface of the $\text{g-C}_3\text{N}_4$ nanotubes.

The photocurrents of the bulk $\text{g-C}_3\text{N}_4$ and the $\text{g-C}_3\text{N}_4$ nanotubes are measured to further study about the separation and transfer efficiency of photogenerated electron-hole pairs, as shown in Fig. 6c. The $\text{g-C}_3\text{N}_4$ nanotubes show higher photocurrent response than that of the bulk $\text{g-C}_3\text{N}_4$. The photocurrents of the $\text{g-C}_3\text{N}_4$ nanotubes still keep stable after five intermittent on-off irradiation cycles. The increased photocurrent value means that the photogenerated electron-hole pairs in the $\text{g-C}_3\text{N}_4$ nanotubes should separate more effectively, which results in the improvement of photocatalytic activity. The electrochemical impedance spectroscopy (EIS) in Fig. 6d. The larger arc radius signifies a larger charge transfer resistance. In other words, a smaller arc radius has a faster charge transfer rate. Clearly, the $\text{g-C}_3\text{N}_4$ nanotubes exhibit a smaller arc radius than that the bulk $\text{g-C}_3\text{N}_4$ coinciding with the photocurrent-time curve.

The relative energy positions of the conduction band (CB) and valence band (VB) are critical to the transfer of photogenerated electron-hole pairs [75]. As we all know, the position of the VB is directly relative to the oxidative ability of $\text{g-C}_3\text{N}_4$, and the position of the CB is directly relative to the

Fig. 5. (a) Photocatalytic hydrogen evolution with 10 vol% triethanolamine aqueous solution, 3 wt% Pt as a co-catalyst and 0.015 g photocatalysts under visible light irradiation, (b) wavelength dependence of external quantum efficiency for $\text{g-C}_3\text{N}_4$ nanotubes.

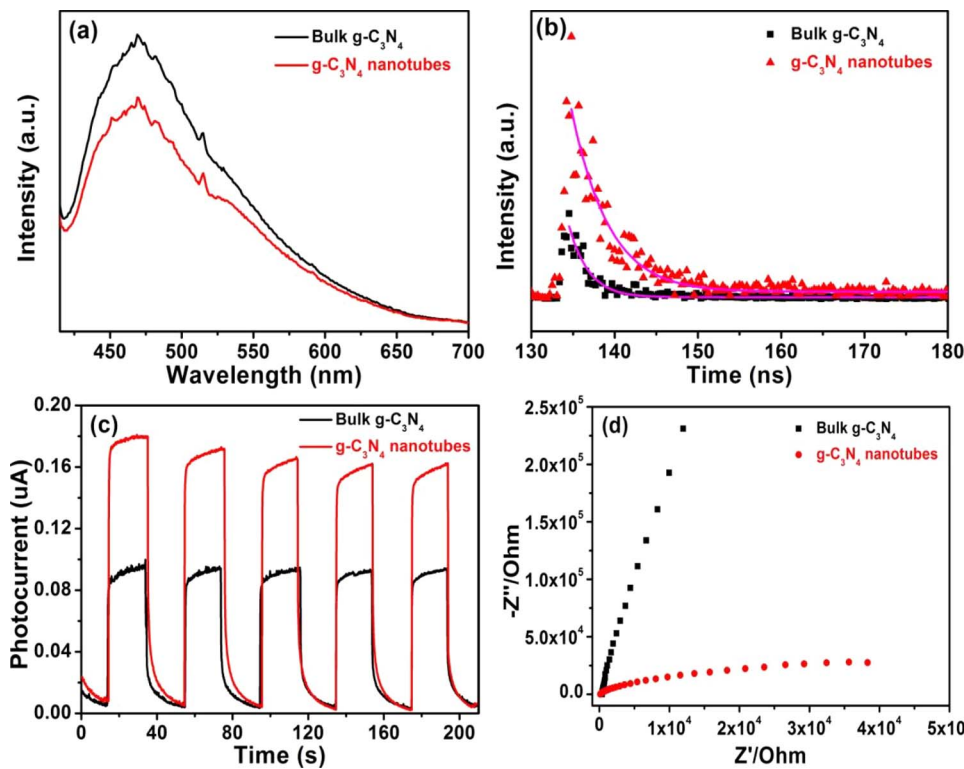


Fig. 6. (a) The PL spectra of the bulk $\text{g-C}_3\text{N}_4$ and the $\text{g-C}_3\text{N}_4$ nanotubes, (b) the fluorescence decay curves of the bulk $\text{g-C}_3\text{N}_4$ and the $\text{g-C}_3\text{N}_4$ nanotubes, (c) Photocurrent responses of the bulk $\text{g-C}_3\text{N}_4$ and the $\text{g-C}_3\text{N}_4$ nanotubes under visible light irradiation, (d) ESI Nyquist plots of the bulk $\text{g-C}_3\text{N}_4$ and the $\text{g-C}_3\text{N}_4$ nanotubes in dark.

reduction ability. The VB of the bulk $\text{g-C}_3\text{N}_4$ and the $\text{g-C}_3\text{N}_4$ nanotubes are determined by the valence band X-ray photoelectron spectroscopy (VB XPS) as shown in Fig. S9a. E_{VB} of the bulk $\text{g-C}_3\text{N}_4$ and the $\text{g-C}_3\text{N}_4$ nanotubes is estimated to be 1.74 eV and 2.02 eV, respectively. According to the DRS analysis in Fig. 4b, E_g of the bulk $\text{g-C}_3\text{N}_4$ and the $\text{g-C}_3\text{N}_4$ nanotubes is estimated to be 2.78 eV and 2.75 eV, respectively. The values of E_{CB} are evaluated to be about -1.04 eV and -0.73 eV by the formula ($E_{\text{CB}} = E_{\text{VB}} - E_g$). Hence, the band gap of the $\text{g-C}_3\text{N}_4$ nanotubes got narrower than that of bulk $\text{g-C}_3\text{N}_4$, and also caused a downshift of the CB/VB position. There is no doubt that the lower CB position may cause the lower reduction ability, but there are a lot of factors affecting the photocatalytic hydrogen evolution. The higher transfer and separation efficiency of the photogenerated electron-hole pairs are probably the major reasons. According to the analysis results above, the well-organized tubular structure and the abundant nitrogen defects can deeply facilitate transfer and separation efficiency of the photogenerated electron-hole pairs. The photocatalytic hydrogen evolution mechanism is shown in Fig. S6. Under visible light irradiation, the photogenerated electron-hole pairs are separated in the $\text{g-C}_3\text{N}_4$ nanotubes. Then due to the unique advantage of fast and long-distance electron transport, the electrons on the conduction band can rapidly transfer to the surface of $\text{g-C}_3\text{N}_4$ nanotubes and couple with Pt. Finally, H^+ unites with the electrons to produce H_2 . Meanwhile, the holes react with triethanolamine to produce the

oxidation product. In addition, the electron spin resonance (ESR) technique and trapping experiment are performed to reveal the main active oxygen species in the photocatalytic process, and the photocatalytic degradation mechanism of $\text{g-C}_3\text{N}_4$ nanotubes is also discussed in Fig. S9b.

3.7. Photoelectrochemical detection of MB

On the basis that the $\text{g-C}_3\text{N}_4$ nanotubes have rapid migration and separation efficiency of photogenerated electron-hole pairs, a photoelectrochemical sensing platform based on $\text{g-C}_3\text{N}_4$ nanotubes/ITO is designed to detect MB. The photocurrent intensity is directly related to the concentration of MB, so the concentration of target MB could be detected by observing the variation of photocurrent. Fig. 7a is the photocurrent response curves of the $\text{g-C}_3\text{N}_4$ nanotubes/ITO electrodes with different concentrations of MB under illumination. As can be seen from the graph, the photocurrent intensity gradually decreases with the increase of MB concentration. In Fig. 7b, it shows a good linear relationship between the photocurrent intensity and MB concentration ranging from 0.2–15.4 ng/mL. The linear fitting equation is $I = 0.0087C_{\text{MB}} + 0.0112$, and the linear correlation was 0.9903. In addition, the detection limit is 0.067 ng/mL ($S/N = 3$). All the results indicate that the photoelectrochemical sensor based on the $\text{g-C}_3\text{N}_4$ nanotubes could be successfully constructed with rapid and sensitive detection of MB.

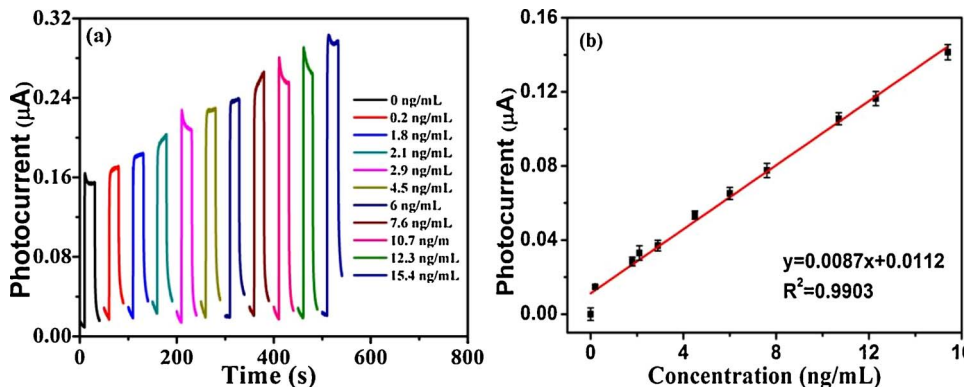


Fig. 7. (a) Photocurrent responses at $\text{g-C}_3\text{N}_4$ nanotubes/ITO electrode in 0.1 mol L^{-1} pH 7.0 phosphate buffer solution toward MB at increasing concentrations at 0 V with visible light excitation; (b) The linear calibration curve used for MB detection.

4. Conclusions

In summary, the rod-like supramolecular intermediate is successfully fabricated via molecular self-assembly. Then the high-yield defect-engineered g-C₃N₄ nanotubes can be obtained by directly heating the supramolecular intermediate. The photocatalytic activity of the g-C₃N₄ nanotubes is enormously enhanced through nanostructure design and defect engineering, attributed to several advantages: (a) faster and longer-distance electron transport, (b) better optical absorption, (c) faster transfer and higher separation efficiency of the photogenerated electron-hole pairs, (d) larger surface area, and (e) longer fluorescence lifetime. This study may provide a guide for designing controllable nanostructures for high performance photocatalyst by molecular self-assembly, and promote the use of supramolecular intermediate as precursor to synthesize highly powerful g-C₃N₄ photocatalyst.

Acknowledgements

This work was supported by National Nature Science Foundation of China (21476097, 21776118), six talent peaks project in Jiangsu Province (2014-JNHB-014). A Project Funded by the Priority Academic Program Development of Jiangsu Higher Education Institutions.

Appendix A. Supplementary data

Supplementary data associated with this article can be found, in the online version, at <https://doi.org/10.1016/j.apcatb.2017.11.041>.

References

- [1] G.P. Dong, Y.H. Zhang, Q.W. Pan, J.R. Qiu, *Photochem. Photobiol. C* 20 (2014) 33–50.
- [2] J.C. Bian, L.F. Xi, C. Huang, K.M. Lange, R.-Q. Zhang, M. Shalom, *Adv. Energy Mater.* 6 (2016) 1600263.
- [3] X.P. Dong, F.X. Cheng, *J. Mater. Chem. A* 3 (2015) 23642–23652.
- [4] Y. Kang, Y. Yang, L.C. Yin, X. Kang, L. Wang, G. Liu, H.M. Cheng, *Adv. Mater.* 28 (2016) 6471–6477.
- [5] H. Yu, R. Shi, Y. Zhao, T. Bian, Y. Zhao, C. Zhou, G.I.N. Waterhouse, L.Z. Wu, C.H. Tung, T. Zhang, *Adv. Mater.* 29 (2017).
- [6] S.C. Yan, Z.S. Li, Z.G. Zou, *Langmuir* 25 (2009) 10397–10401.
- [7] H.H. Ji, F. Chang, X.F. Hu, W. Qin, J.W. Shen, *Chem. Eng. J.* 218 (2013) 183–190.
- [8] G.G. Zhang, J.S. Zhang, M.W. Zhang, X.C. Wang, *J. Mater. Chem.* 22 (2012) 8083–8091.
- [9] F. Dong, Z. Wang, Y. Sun, W.K. Ho, H. Zhang, *J. Colloid Interface Sci.* 401 (2013) 70–79.
- [10] H. Xu, J.J. Yi, X.J. She, Q. Liu, L. Song, S.M. Chen, Y.C. Yang, Y.H. Song, R. Vajtai, J. Lou, H.M. Li, S.Q. Yuan, J.J. Wu, P.M. Ajayan, *Appl. Catal. B: Environ.* 220 (2018) 379–385.
- [11] Q. Han, B. Wang, J. Gao, Z.H. Cheng, Y. Zhao, Z.P. Zhang, L.T. Qu, *ACS Nano* 10 (2016) 2745–2751.
- [12] Y.F. Li, R.X. Jin, Y. Xing, J.Q. Li, S.Y. Song, X.C. Liu, M. Li, R.C. Jin, *Adv. Energy Mater.* 6 (2016) 1601273.
- [13] G.G. Zhang, S.H. Zang, L.H. Lin, Z.A. Lan, G.S. Li, X.C. Wang, *ACS Appl. Mater. Interfaces* 8 (2016) 2287–2296.
- [14] Y.P. Wang, Y.K. Li, W. Ju, J.C. Wang, H.C. Yao, L. Zhang, J.S. Wang, Z.J. Li, *Carbon* 102 (2016) 477–486.
- [15] M. Zhang, X.J. Bai, D. Liu, J. Wang, Y.F. Zhu, *Appl. Catal. B* 164 (2015) 77–81.
- [16] X.L. Wang, W.Q. Fang, W.Q. Liu, Y. Jia, D.W. Jing, Y. Wang, L.Y. Yang, X.Q. Gong, Y.F. Yao, H.G. Yang, X.D. Yao, *J. Mater. Chem. A* 5 (2017) 19227–19236.
- [17] S.W. Zhang, J.X. Li, M.Y. Zeng, J. Li, J.Z. Xu, X.K. Wang, *Chemistry* 20 (2014) 9805–9812.
- [18] D.L. Jiang, T.Y. Wang, Q. Xu, D. Li, S.C. Meng, M. Chen, *Appl. Catal. B* 201 (2017) 617–628.
- [19] G.G. Liu, G.X. Zhao, W. Zhou, Y.Y. Liu, H.B. Pang, H. Zhang, D. Hao, X.G. Meng, P. Li, T. Kako, J.H. Ye, *Adv. Funct. Mater.* 26 (2016) 6822–6829.
- [20] W.J. Jiang, W.J. Luo, J. Wang, M. Zhang, Y.F. Zhu, *J. Photochem. Photobiol. C* 28 (2016) 87–115.
- [21] S.W. Cao, J.X. Low, J.G. Yu, M. Jaroniec, *Adv. Mater.* 27 (2015) 2150–2176.
- [22] X.J. She, J.J. Wu, J. Zhong, H. Xu, Y.C. Yang, R. Vajtai, J. Lou, Y. Liu, D.L. Du, H.M. Li, P.M. Ajayan, *Nano Energy* 27 (2016) 138–146.
- [23] K. Zhang, L. Wang, X. Sheng, M. Ma, M.S. Jung, W. Kim, H. Lee, J.H. Park, *Adv. Energy Mater.* 6 (2016) 1502352.
- [24] H.J. Li, D.J. Qian, M. Chen, *ACS Appl. Mater. Interfaces* 7 (2015) 25162–25170.
- [25] Y.J. Cui, Z.X. Ding, X.Z. Fu, X.C. Wang, *Angew. Chem. Int. Ed.* 51 (2012) 11814–11818.
- [26] Q.X. Guo, Y. Xie, X.J. Wang, S.Y. Zhang, T. Hou, S.C. Lv, *Chem. Commun.* (2004) 26–27.
- [27] J. Li, C.B. Cao, H.S. Zhu, *Nanotechnology* 18 (2007) 115605.
- [28] Z. Yang, Y.J. Zhang, Z. Schnepp, *J. Mater. Chem. A* 3 (2015) 14081–14092.
- [29] X.F. Lu, H.J. Wang, S.Y. Zhang, D.L. Cui, Q.L. Wang, *Solid State Sci.* 11 (2009) 428–432.
- [30] Z.J. Huang, F.B. Li, B.F. Chen, G.Q. Yuan, *RSC Adv.* 5 (2015) 102700–102706.
- [31] Z.W. Tong, D. Yang, Y.Y. Sun, Y.H. Nan, Z.Y. Jiang, *Small* 12 (2016) 4093–4101.
- [32] S.E. Guo, Z.P. Deng, M.X. Li, B.J. Jiang, C.G. Tian, Q.J. Pan, H.G. Fu, *Angew. Chem. Int. Ed.* 55 (2016) 1830–1834.
- [33] Y.S. Jun, E.Z. Lee, X. Wang, W.H. Hong, G.D. Stucky, A. Thomas, *Adv. Funct. Mater.* 23 (2013) 3661–3667.
- [34] Y.L. Liao, S.M. Zhu, J. Ma, Z.H. Sun, C. Yin, C.L. Zhu, X.H. Lou, D. Zhang, *ChemCatChem* 6 (2014) 3419–3425.
- [35] M. Shalom, M. Guttentag, C. Fettkenhauer, S. Inal, D. Neher, A. Llobet, M. Antonietti, *Chem. Mater.* 26 (2014) 5812–5818.
- [36] M. Shalom, S. Inal, C. Fettkenhauer, D. Neher, M. Antonietti, *J. Am. Chem. Soc.* 135 (2013) 7118–7121.
- [37] K. Li, X. Xie, W.D. Zhang, *ChemCatChem* 8 (2016) 2128–2135.
- [38] N.A. Wasio, R.C. Quardokus, R.P. Forrest, C.S. Lent, S.A. Corcelli, J.A. Christie, K.W. Henderson, S.A. Kandel, *Nature* 507 (2014) 86–89.
- [39] Y. Ishida, L. Chabanne, M. Antonietti, M. Shalom, *Langmuir* 30 (2014) 447–451.
- [40] J.S. Xu, M. Antonietti, *J. Am. Chem. Soc.* 139 (2017) 6026–6029.
- [41] J.S. Xu, H. Wang, C. Zhang, X.F. Yang, S.W. Cao, J.G. Yu, M. Shalom, *Angew. Chem. Int. Ed.* (2017).
- [42] Y.F. Guo, J. Li, Y.P. Yuan, L. Li, M.Y. Zhang, C.Y. Zhou, Z.Q. Lin, *Angew. Chem. Int. Ed.* 55 (2016) 14693–14697.
- [43] M.K. Bhunia, K. Yamauchi, K. Takanabe, *Angew. Chem. Int. Ed.* 53 (2014) 11001–11005.
- [44] J. Gao, Y. Zhou, Z.S. Li, S.C. Yan, N.Y. Wang, Z.G. Zou, *Nanoscale* 4 (2012) 3687–3692.
- [45] H. Pan, Y.W. Zhang, V.B. Shenoy, H. Gao, *ACS Catal.* 1 (2011) 99–104.
- [46] G. Arrachart, C. Carcel, P. Trens, J.J. Moreau, M. Wong Chi Man, *Chemistry* 15 (2009) 6279–6288.
- [47] J. Fu, B. Zhu, C. Jiang, B. Cheng, W. You, J. Yu, *Small* 13 (2017) 1603938.
- [48] Z. Mo, X.J. She, Y.P. Li, L. Liu, L.Y. Huang, Z.G. Chen, Q. Zhang, H. Xu, H.M. Li, *RSC Adv.* 5 (2015) 101552–101562.
- [49] X.J. Bai, L. Wang, R.L. Zong, Y.F. Zhu, *J. Phys. Chem. C* 117 (2013) 9952–9961.
- [50] G.L. Chai, C.S. Lin, J. Wei, M.Y. Zhang, W.D. Cheng, *Phys. Chem. Chem. Phys.* 14 (2012) 835–839.
- [51] S.P. Wang, C.J. Li, T. Wang, P. Zhang, A. Li, J.L. Gong, *J. Mater. Chem. A* 2 (2014) 2885.
- [52] H. Xu, J. Yan, X.J. She, L. Xu, J.X. Xia, Y.G. Xu, Y.H. Song, L.Y. Huang, H.M. Li, *Nanoscale* 6 (2014) 1406–1415.
- [53] P. Niu, L.L. Zhang, G. Liu, H.M. Cheng, *Adv. Funct. Mater.* 22 (2012) 4763–4770.
- [54] Q. Han, B. Wang, Y. Zhao, C.G. Hu, L.T. Qu, *Angew. Chem. Int. Ed.* 54 (2015) 11433–11437.
- [55] X.J. She, H. Xu, Y.G. Xu, J. Yan, J.X. Xia, L. Xu, Y.H. Song, Y. Jiang, Q. Zhang, H.M. Li, *J. Mater. Chem. A* 2 (2014) 2563–2570.
- [56] X.J. She, H. Xu, H.F. Wang, J.X. Xia, Y.H. Song, J. Yan, Y.G. Xu, Q. Zhang, D.L. Du, H.M. Li, *Dalton Trans.* 44 (2015) 7021–7031.
- [57] J.S. Zhang, M.W. Zhang, C. Yang, X.C. Wang, *Adv. Mater.* 26 (2014) 4121–4126.
- [58] V.W.-h. Lau, V.W.-z. Yu, F. Ehrat, T. Botari, I. Moudrakovski, T. Simon, V. Duppel, E. Medina, J. Stolarczyk, J. Feldmann, V. Blum, B.V. Lotsch, *Adv. Energy Mater.* (2017) 1602251.
- [59] X.J. She, L. Liu, H.Y. Ji, Z. Mo, Y.P. Li, L.Y. Huang, D.L. Du, H. Xu, H.M. Li, *Appl. Catal. B* 187 (2016) 144–153.
- [60] J. Yan, Z.G. Chen, H.Y. Ji, Z. Liu, X. Wang, Y.G. Xu, X.J. She, L.Y. Huang, L. Xu, H. Xu, H.M. Li, *Chemistry* 22 (2016) 4764–4773.
- [61] D.J. Martin, *Angew. Chem. Int. Ed.* 53 (2014) 9240–9245.
- [62] H.C. Lan, L.L. Li, J.H. Liu, X.Q. An, F. Liu, C.B. Chen, J. Qu, *Appl. Catal. B* 204 (2017) 49–57.
- [63] G.G. Zhang, M.W. Zhang, X.X. Ye, X.Q. Qiu, S. Lin, X.C. Wang, *Adv. Mater.* 26 (2014) 805–809.
- [64] P. Niu, L.C. Yin, Y.Q. Yang, G. Liu, H.M. Cheng, *Adv. Mater.* 26 (2014) 8046–8052.
- [65] X.C. Wang, K. Maeda, X.F. Chen, K. Takanabe, K. Domen, Y.D. Hou, X.Z. Fu, M. Antonietti, *J. Am. Chem. Soc.* 131 (2009) 1680–1681.
- [66] P. Niu, G. Liu, H.M. Cheng, *J. Phys. Chem. C* 116 (2012) 11013–11018.
- [67] X.H. Li, J.S. Zhang, X.F. Chen, A. Fischer, A. Thomas, M. Antonietti, X.C. Wang, *Chem. Mater.* 23 (2011) 4344–4348.
- [68] J. Liu, J.H. Huang, D. Dontosova, M. Antonietti, *RSC Adv.* 3 (2013) 22988.
- [69] J.S. Zhang, F.S. Guo, X.C. Wang, *Adv. Funct. Mater.* 23 (2013) 3008–3014.
- [70] G.H. Dong, W.K. Ho, C.Y. Wang, *J. Mater. Chem. A* 3 (2015) 23435.
- [71] G.S. Kumar, R. Roy, D. Sen, U.K. Ghorai, R. Thapa, N. Mazumder, S. Saha, K.K. Chattopadhyay, *Nanoscale* 6 (2014) 3384–3391.
- [72] D. Das, D. Banerjee, D. Pahari, U.K. Ghorai, S. Sarkar, N.S. Das, K.K. Chattopadhyay, J. Lumin. 185 (2017) 155–165.
- [73] P.J. Yang, H.H. Ou, Y.X. Fang, X.C. Wang, *Angew. Chem. Int. Ed.* 56 (2017) 3992–3996.
- [74] P. Zhang, T. Wang, X.X. Chang, J.L. Gong, *Acc. Chem. Res.* 49 (2016) 911–921.
- [75] B. Wang, J. Di, P.F. Zhang, J.X. Xiang, S. Dai, H.M. Li, *Appl. Catal. B* 206 (2017) 127–135.